AIP | Physics of Plasmas

#1 JOURNAL IN 2014 GOOGLE SCHOLAR METRICS FOR THE PLASMA & FUSION CATEGORY

Recent advances in long-pulse high-confinement plasma operations in Experimental Advanced Superconducting Tokamaka)

H. Y. Guo, J. Li, B. N. Wan, X. Z. Gong, Y. F. Liang, G. S. Xu, X. D. Zhang, S. Y. Ding, K. F. Gan, J. S. Hu, L. Q. Hu, S. C. Liu, J. P. Qian, Y. W. Sun, H. Q. Wang, L. Wang, T. Y. Xia, B. J. Xiao, L. Zeng, Y. P. Zhao, P. Denner , J. R. Ferron, A. M. Garofalo, C. T. Holcomb, A. W. Hyatt, G. L. Jackson, A. Loarte, R. Maingi, J. E. Menard, M. Rack, W. M. Solomon, X. Q. Xu, M. Van Zeeland, X. L. Zou, and EAST Team

Citation: Physics of Plasmas **21**, 056107 (2014); doi: 10.1063/1.4872195

View online: http://dx.doi.org/10.1063/1.4872195

View Table of Contents: http://scitation.aip.org/content/aip/journal/pop/21/5?ver=pdfcov

Published by the AIP Publishing

Articles you may be interested in

Observation of pedestal turbulence in edge localized mode-free H-mode on experimental advanced superconducting tokamak
Phys. Plasmas **21**, 102504 (2014); 10.1063/1.4897923

Edge-coherent-mode nature of the small edge localized modes in Experimental Advanced Superconducting Tokamak
Phys. Plasmas **21**, 092511 (2014); 10.1063/1.4896237

Lower hybrid current drive and ion cyclotron range of frequencies heating experiments in H-mode plasmas in Experimental Advanced Superconducting Tokomak
Phys. Plasmas **21**, 061501 (2014); 10.1063/1.4884356

Influence of helium puff on divertor asymmetry in Experimental Advanced Superconducting Tokamak
Phys. Plasmas **21**, 022509 (2014); 10.1063/1.4863843

Advanced tokamak research with integrated modeling in JT-60 Upgradea)
Phys. Plasmas **17**, 056112 (2010); 10.1063/1.3327917

PFEIFFER VACUUM

VACUUM SOLUTIONS FROM A SINGLE SOURCE

Pfeiffer Vacuum stands for innovative and custom vacuum solutions worldwide, technological perfection, competent advice and reliable service.

This article is copyrighted as indicated in the article. Reuse of AIP content is subject to the terms at: http://scitation.aip.org/termsconditions. Downloaded to IP: 134.94.122.242 On: Tue, 23 Jun 2015 11:38:54

PHYSICS OF PLASMAS **21**, 056107 (2014)

Recent advances in long-pulse high-confinement plasma operations in Experimental Advanced Superconducting Tokamak[a)]

H. Y. Guo,[1,2,b)] J. Li,[1] B. N. Wan,[1,c)] X. Z. Gong,[1] Y. F. Liang,[1,3] G. S. Xu,[1] X. D. Zhang,[1] S. Y. Ding,[1] K. F. Gan,[1] J. S. Hu,[1] L. Q. Hu,[1] S. C. Liu,[1] J. P. Qian,[1] Y. W. Sun,[1] H. Q. Wang,[1] L. Wang,[1] T. Y. Xia,[1] B. J. Xiao,[1] L. Zeng,[1] Y. P. Zhao,[1] P. Denner,[3] J. R. Ferron,[4] A. M. Garofalo,[4] C. T. Holcomb,[5] A. W. Hyatt,[4] G. L. Jackson,[4] A. Loarte,[6] R. Maingi,[7,8] J. E. Menard,[7] M. Rack,[3] W. M. Solomon,[7] X. Q. Xu,[5] M. Van Zeeland,[4] X. L. Zou,[9] and EAST Team[1]

[1]*Institute of Plasma Physics, Chinese Academy of Sciences, P.O. Box 1126, Hefei 230031, People's Republic of China*
[2]*Tri Alpha Energy, Inc., P.O. Box 7010, Rancho Santa Margarita, California 92688, USA*
[3]*Forschungszentrum Jülich GmbH, Association EURATOM-FZ Jülich, Institut für Energie- und Klimaforschung-Plasmaphysik, Trilateral Euregio Cluster, D-52425 Jülich, Germany*
[4]*General Atomics, P. O. Box 85608, San Diego, California 92186, USA*
[5]*Lawrence Livermore National Laboratory, Livermore, California 94550, USA*
[6]*ITER Organization, Route de Vinon sur Verdon, 13115 St Paul Lez Durance, France*
[7]*Princeton Plasma Physics Laboratory, P. O. Box 451, Princeton, New Jersey 08543, USA*
[8]*Oak Ridge National Laboratory, Oak Ridge, Tennessee 37831, USA*
[9]*CEA, IRFM, F-13108 Saint-Paul-lez-Durance, France*

(Received 29 November 2013; accepted 31 January 2014; published online 30 April 2014)

A long-pulse high confinement plasma regime known as H-mode is achieved in the Experimental Advanced Superconducting Tokamak (EAST) with a record duration over 30 s, sustained by Lower Hybrid wave Current Drive (LHCD) with advanced lithium wall conditioning and divertor pumping. This long-pulse H-mode plasma regime is characterized by the co-existence of a small Magneto-Hydrodynamic (MHD) instability, i.e., Edge Localized Modes (ELMs) and a continuous quasi-coherent MHD mode at the edge. We find that LHCD provides an intrinsic boundary control for ELMs, leading to a dramatic reduction in the *transient* power load on the vessel wall, compared to the standard Type I ELMs. LHCD also induces edge plasma ergodization, broadening heat deposition footprints, and the heat transport caused by ergodization can be actively controlled by regulating edge plasma conditions, thus providing a new means for *stationary* heat flux control. In addition, advanced tokamak scenarios have been newly developed for high-performance long-pulse plasma operations in the next EAST experimental campaign. © *2014 AIP Publishing LLC*. [http://dx.doi.org/10.1063/1.4872195]

I. INTRODUCTION

Long-pulse plasma operation has been demonstrated in various fusion experiments.[1] It is urgently required to address critical issues facing long-pulse operations that entail high input power while maintaining high energy confinement.[2] A key challenge facing high-power long-pulse operations is to maintain a fusion plasma with adequate performance while preventing its damage to the Plasma Facing Components (PFCs), especially divertors, which provide an essential exhaust system for handling power flow from the core plasma and removing helium ash in a D-T fusion reactor.[3] Thus, it is essential to simultaneously control heat load on PFCs, neutral particle recycling, and impurity contamination resulting from plasma-wall interactions.[1]

The Experimental Advanced Superconducting Tokamak (EAST, formerly named HT-7U)[4] was built to demonstrate high-power, long-pulse operations, with major radius $R \sim 1.9$ m, minor radius $a \sim 0.5$ m, and expected pulse length up to 1000 s. All the magnetic coils, including 16 toroidal field coils, 6 poloidal field coils, and 6 central solenoid coils, are superconductors made from niobium-titanium alloy embedded in copper. The maximum plasma current and toroidal field achieved in EAST are $I_p = 1$ MA, $B_T = 3.5$ T, which can be further raised to $I_p = 1.5$ MA and $B_T = 4$ T by reducing the temperature of the superconducting magnets from presently 4.5 K to ~3.8 K. EAST has an ITER-like D-shaped cross section with two symmetric divertors at the top and bottom, accommodating both single null (SN) and double null (DN) divertor configurations, as shown in Fig. 1. In addition, EAST adopts the ITER-like heating schemes, i.e., with dominant electron heating, provided by Radio Frequency (RF) heating, including both Lower Hybrid Current Drive (LHCD) and Ion Cyclotron Resonance Heating (ICRH), which produce low momentum injection, unlike many of the present tokamaks. Thus, EAST experiments can provide useful information on some physics and engineering issues for ITER.

A great effort has been made on EAST to improve its capability for long-pulse, high-performance plasma operations

---

[a)] Paper UI2 5, Bull. Am. Phys. Soc. **58**, 321 (2013).
[b)] Invited speaker.
[c)] Electronic mail: bnwan@ipp.ac.cn

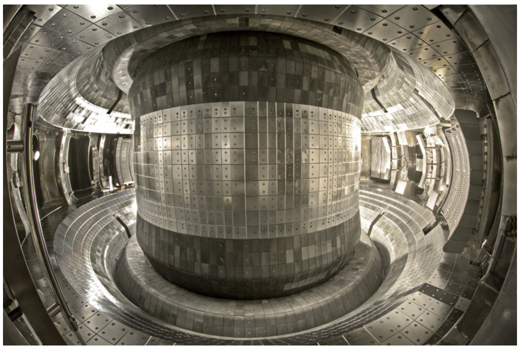

FIG. 1. Internal view of EAST superconducting tokamak with molybdenum plasma facing components inside the main chamber and two toroidally symmetric divertors covered with graphite tiles at top and bottom.

over the last few years. Section II gives a brief description of the technical development and recent upgrade of the in-vessel components, heating and current drive systems, as well as new and upgraded diagnostic capabilities. This enabled the achievement of a high confinement mode, i.e., H-mode,[5] with a pulse duration over 30 s, with predominant heating and current drive from LHCD and extensive Lithium (Li) wall conditioning, hence setting a record for long-pulse H-mode operations,[6–9] during the last EAST experimental campaign in 2012. The distinct features of this new long-pulse H-mode regime is shown in Sec. III. Many new and interesting physics results have been obtained in the quest for long-pulse operations. Section IV offers evidence that the LHCD provides a flexible boundary control of a repetitive edge Magneto-Hydrodynamic (MHD) instability, i.e., Edge Localized Mode (ELMs), which is ubiquitous in H-mode plasmas, by driving the current in the scrape-off layer (SOL), producing a three-dimensional (3D) perturbation of edge magnetic fields. This leads to a dramatic reduction in ELM amplitude and transient power deposition on the divertor target plates. The change in the edge magnetic topology induced by LHCD also facilitates the stationary heat exhaust by broadening power deposition footprints. Another new finding is that the small ELMs are accompanied by a new, quasi-coherent MHD mode at the edge, termed Edge Coherent Mode (ECM), throughout the long-pulse H-mode phase, further facilitating power and particle exhaust, as presented in Sec. V, where modeling results from GYRO simulations are also presented to better understand the nature of ECMs. In addition, the magnetic configurations appear to exert a significant influence on long-pulse operations, via coupling to divertor pumping, as discussed in Sec. VI. Section VII presents the newly developed steady-state advanced tokamak scenarios for EAST, in collaboration with the DIII-D team at General Atomics. Finally, Sec. VIII presents a summary and conclusions.

II. EAST CAPABILITIES

To improve power handling and particle exhaust for long-pulse operations, EAST carried out an extensive upgrade of its internal PFCs during the last shutdown in 2011, replacing carbon tiles on the main chamber wall and divertor surface by molybdenum (Mo) tiles, except for those near the strike points, with the enhanced baking capability over 250 °C. All PFCs can be actively water cooled, allowing for a steady-state heat load of 2 MW/m^2. A large capacity divertor cryopump is situated underneath the bottom outboard divertor with a pumping speed of 76 m^3/s for D$_2$ and 107 m^3/s for hydrogen, which provides an essential tool for particle exhaust in long-pulse discharges.

To control recycling and facilitate density maintenance, a large effort has been devoted to the development of wall conditioning techniques suitable for superconducting tokamak operations, such as Ion Cyclotron Resonant Frequency (ICRF) wave-assisted Glow Discharge Cleaning (GDC) and high frequency GDC. In particular, we have developed an advanced wall conditioning technique by introducing conventional Lithium (Li) evaporation into ICRF wave-assisted plasma discharges[10] to improve the uniformity of Li coverage on the wall in the presence of toroidal magnetic fields. Li wall conditioning has proven to be the most effective method employed in EAST to control hydrogenic recycling, lowering the recycling coefficient down to $R_c \sim 0.9$ by a fresh Li coating, which exhibits a strong coating effect persisting over ∼100 shot-seconds.[8] In addition, real-time injection of Li powder has been demonstrated in EAST, in collaboration with Princeton Plasma Physics Laboratory (PPPL),[11] which offers an attractive real-time wall conditioning technique for long-pulse plasmas.

The current drive and heating are predominantly provided by the Lower Hybrid Waves (LHW) at the frequency of 2.45 GHz with a total power of 4 MW. In addition, EAST is equipped with an ICRH system with tunable frequency ranging from 20 to 70 MHz, using the hydrogen-minority heating scheme. It consists of two double-strap antennas, each delivering 3 MW of power. EAST has a flexible feedback Plasma Control System (PCS) for plasma equilibrium and current drive and heating needs. The PCS was further improved to enable fast change and accurate control of magnetic configurations and plasma shapes, i.e., Upper Singer Null (USN), DN, or Lower Single Null (LSN), using the advanced iso-flux control technique for selected control points on the plasma boundary, including X-points or strike points with real-time equilibrium reconstruction (RTEFIT), developed by joint efforts from the DIII-D and EAST plasma control groups.[12] This allows for periodic change of the divertor configurations with strike-point sweeping to facilitate power exhaust and density maintenance in long-pulse discharges. The poloidal field power supply and plasma control system have also been upgraded during the last shutdown to provide more flexibilities and large safety margins, extending the plasma operation space. In addition, a new pellet injection system and a new Supersonic Molecular Beam Injection (SMBI) system have been implemented for ELM mitigation and fast density feedback control.

There are presently over 40 matured diagnostics on EAST. Many key diagnostics, such as Thomson scattering, Interferometry, electron cyclotron emission, reflectometer were completely refurbished and upgraded during the last shutdown for detailed profile measurements. In addition, two

X-ray Crystal Spectrometers (XCS), polarimetry, and CO_2 Laser Collective Thomson Scattering (LCTS) have been developed to provide new information on ion and electron temperature profiles, toroidal and poloidal plasma rotation, current profiles, as well as turbulence structures in the core plasma, significantly improving diagnostic capabilities for physics studies. A large effort has also been made on the development of edge plasma diagnostics. Figure 2 shows a sketch of some key edge diagnostics in EAST, including the following systems. (1) Divertor triple probe system: 222 Langmuir probes embedded in the divertor target plates for the measurement of plasma density, temperature, particle, and heat flux profiles along the target plates. (2) Fast reciprocating probe system: two fast moving reciprocating Langmuir probes are located at the outboard midplane, nearly 90° apart, providing edge plasma profile, rotation, and turbulence measurements, which can penetrate $\sim$4 cm inside the separatrix. (3) Spectroscopy: including a 35-channel photodiode array (PDA) with interference filter (at 659.3 nm with FWHM 10 nm) for monitoring D_α emissions, viewing the inner target and dome surface of the low divertor from the outer midplane through the in-vessel reflection mirrors, a 12-channel filterscope system viewing the lower divertor from the outer midplane for simultaneous measurement of D_α, CIII, and HeII emissions with high-time resolution (100 kHz), and high resolution spectrometers (SP750) for monitoring various impurity line emissions in the divertor SOL. (4) Gas Puffing Imaging (GPI): two GPI systems symmetric about the midplane to view detailed turbulence structures at the edge. In addition, an Infra-Red (IR) camera system views simultaneously the upper, lower divertors, LHW antennas, and movable limiter.

EAST is also equipped with a multi-purpose gas puffing system, which allows gas fuelling from many different divertor and main chamber locations, i.e., inboard/outboard midplane, inner/outer target, and dome at both top and bottom divertors, as shown in Fig. 2. This, combined with impurity puffing, provides an effective means to actively control power and particle fluxes to the divertor target plates, by generating radiative divertor plasmas.

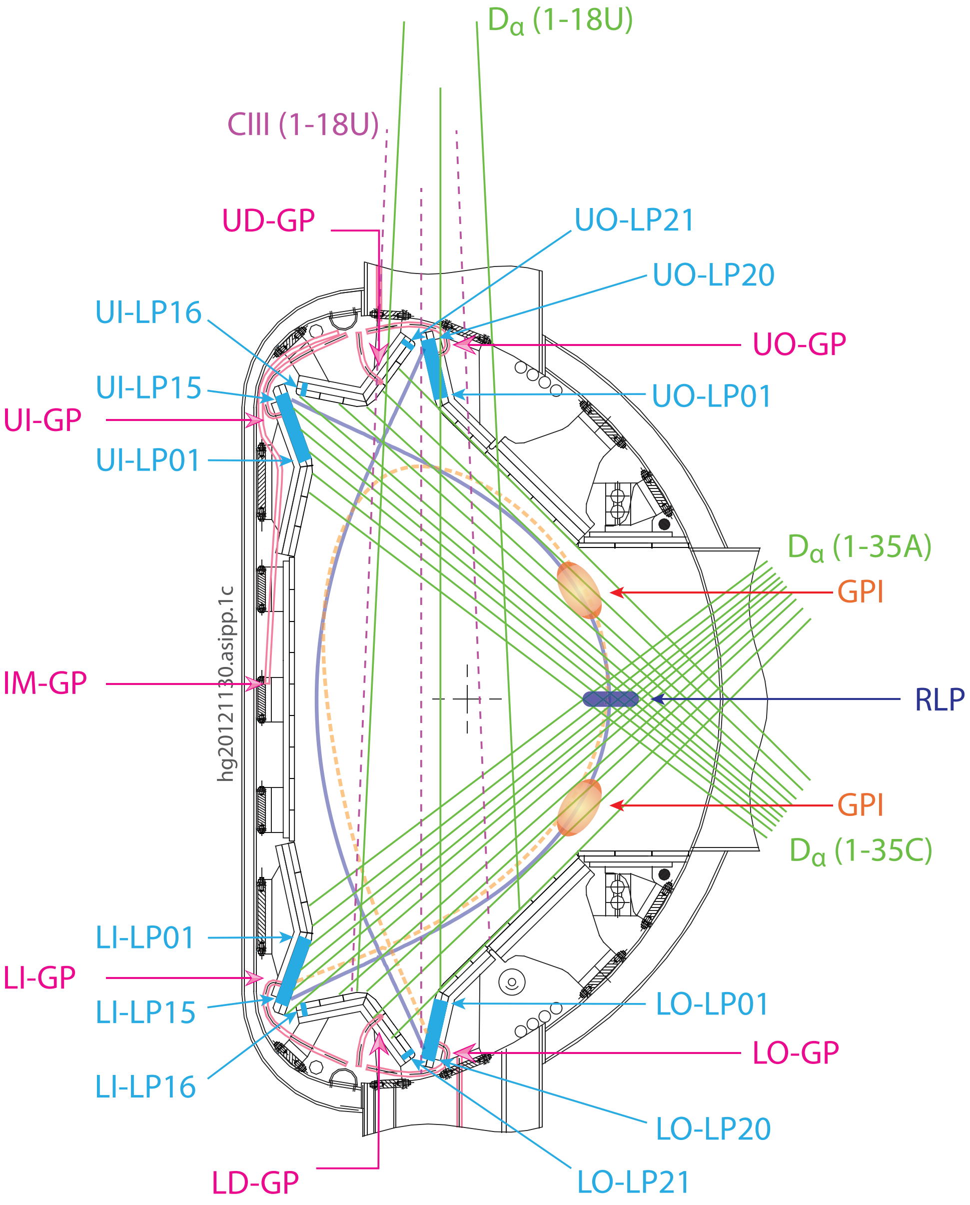

FIG. 2. Poloidal cross section of EAST showing key divertor/SOL diagnostics and divertor gas puff locations. CIII—Line emission of C++ ions; D_α—Balmer-alpha emission of deuterium; GP—Gas Puff Inlet; GPI—Gas Puff Imaging; IM—Inner Midplane; LO(I)—Lower Outboard (Inboard) divertor; LP—Langmuir Probe; RLP—Reciprocating Langmuir Probe; U(L)D—Upper (Lower) divertor Dome; and UO(I)—Upper Outboard (Inboard) divertor.

III. ACHIEVEMENT OF LONG-PULSE H-MODES

To facilitate access to H-modes, Li wall conditioning has been routinely applied in EAST to reduce neutral recycling and impurity radiation. The first H-mode was achieved in EAST in 2010 with LHCD.[13] Due to limited heating power available, H-modes were obtained at marginal heating power with respect to the threshold power needed for the transition from the lower confinement mode, i.e., the L-mode, to the H-mode, achieving stationary H-modes up to 6.4 s. In the recent 2012 campaign, we have achieved highly reproducible, long-pulse H-modes in EAST with the pulse length extended over 30 s, much longer than several tens of the current diffusion time, thus setting a record for the longest H-mode duration to date. These long H-mode plasmas are achieved with auxiliary heating from LHCD and ICRH with $P_{\rm LHCD} = 1$–2 MW and $P_{\rm ICRH} = 0.5$–1.5 MW. The total combined heating power is about 1–3 times the threshold power for the L-H transition. Figure 3 shows the time traces of a typical long-pulse H-mode driven by LHCD with additional ICRH, under the DN divertor configuration with the ion ∇B drift towards the top, $B_T \sim 1.9$ T, $I_p \sim 280$ kA, triangularity $\delta \sim 0.5$, elongation $\kappa \sim 1.7$, $q_{95} \sim 6.8$, and normalized Greenwald density $n_e/n_G \sim 0.5$. Due to strong trapping of hydrogen isotopes with Li wall conditioning, neutral recycling is well controlled and stable plasma density is maintained throughout the long-pulse plasma. Furthermore, Li gettering is also effective at controlling impurity influxes, with the core impurity radiation maintained at an acceptable level in steady state.

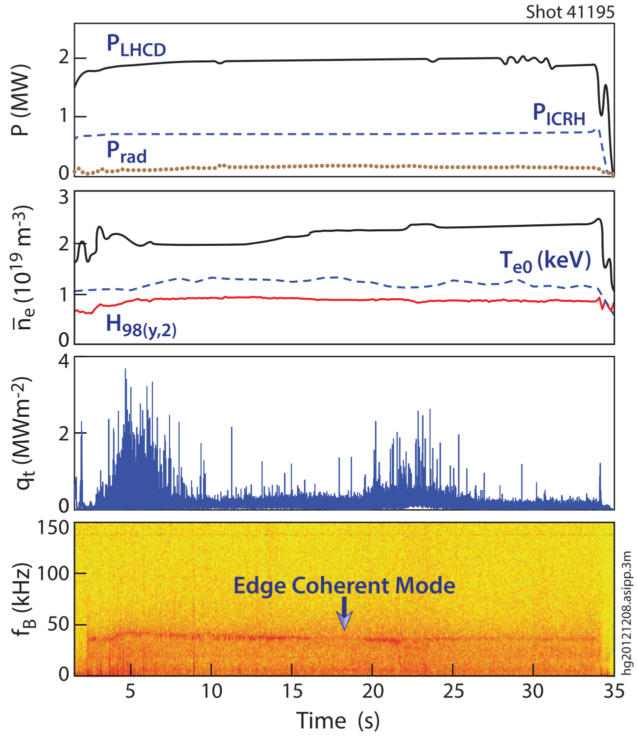

FIG. 3. Demonstration of a high confinement H-mode discharge over 30 s driven by LHCD with additional ICRH. Data shown are injected heating power from LHCD and ICRH, P_{LHCD} and P_{ICRH}, and radiation, P_{rad}; line averaged density, $\bar{n}_e$, central electron temperature, T_{e0}, and H-mode confinement enhancement factor, $H_{98(y,2)}$; divertor target heat flux, q_t, derived from Langmuir probes; and magnetic fluctuation frequency spectrum, f_B, obtained from a Mirnov magnetic pick-up probe near the midplane on the outboard side, showing an edge-coherent mode at $f_B \sim 30$–50 kHz (double null divertor configuration, $B_T = 1.9$ T, $I_p = 0.28$ MA, $n_e/n_{GW} = 0.5$, $\delta = 0.5$, $\kappa = 1.7$, and $q_{95} = 6.8$).

A key feature of long-pulse H-mode plasmas in EAST relies on the achievement of tiny ELMs, leading to a dramatic reduction in energy ejection per ELM event, as compared to the standard ELMs, also referred to as Type I ELMs,[14] which have been adopted as the baseline operation scenario for ITER.[15] Type I ELMy H-modes exhibit an H-mode confinement factor, $H_{98(y,2)} \sim 1$, i.e., about two times L-mode confinement.[16] However, the Type I ELMs, if their amplitude is too large, can eject a significant fraction of plasma-stored energy to the PFCs, posing a serious challenge for long-pulse operations because of excessive reduction of the lifetime of PFCs by erosion and melting.[2] The small ELMs (manifested by spikes in the divertor heat flux, q_t, Fig. 3) in the long-pulse H-mode are rather benign, with a frequency $f_{ELM} \sim 0.5$–1 kHz. Peak heat fluxes on the PFCs from the plasma ejected by the small ELMs are largely below 2 MW/m^2, as determined from the divertor Langmuir probe measurements. The energy loss rate for the small ELMs is typically $<1\%$ of the plasma stored energy, much less than that for the standard ELMs in EAST, i.e., 5%–8%, based on the diamagnetic measurements.[17] This small-ELMy H-mode regime exhibits a confinement quality between Type I and Type III ELMy H-modes,[14] with a confinement enhancement factor, $H_{98(y,2)} \sim 0.9$, similar to the Type II ELMy H-mode.[16,18–22] It is worth noting that with LHCD and Li coating, the long-pulse H-modes have been realized in EAST under otherwise similar operating conditions to the Type II H-modes obtained in other fusion experiments, e.g., with large q_{95}, high δ, large κ, and quasi-DN (with $dR_{sep} < 1$ cm).

Another important facet of the long-pulse H-mode regime is that the small ELMs are accompanied by a continuous quasi-coherent MHD mode at the edge, i.e., ECM, at a frequency $f_{ECM} = 30$–50 kHz throughout the H-mode phase, as seen by external magnetic pick-up probe measurements (Fig. 3) and gas puffing imaging. The ECM saturates at a frequency typically below 50 kHz, sometimes accompanied by a low frequency broadband turbulence. Direct probing using a fast moving reciprocating probe at the midplane of EAST shows that ECM provides continuous particle and heat exhaust during the discharge, hence further facilitating long-pulse operations, as discussed in Sec. V.

Stationary type-I ELMy H-modes have also been obtained in EAST, typically with a lower pedestal collisionality, by further increasing RF heating power.[7] Various means for ELM mitigation have been demonstrated to be compatible with long-pulse operation, including SMBI,[23] as well as innovative solid Li granule injection.[24]

IV. INTRINSIC EDGE CONTROL WITH LHCD

A. Modification of ELM pattern with LHCD

The long-pulse H-mode was achieved in EAST with predominantly LHCD, assisted with ICRH. We have recently discovered that LHCD induces a profound change in the magnetic topology of the edge plasma by driving Helical Current Filaments (HCFs) on the magnetic field lines in the SOL,[25] leading to a 3D distortion of the edge magnetic topology, similar to the application of Resonant Magnetic Perturbations (RMPs) using external magnetic field coils.[26–31] The 3D structure and amplitude of the HCFs driven by LHCD have been measured in EAST by two tangential visible CCD cameras viewing the opposite sides of the torus and a set of Mirnov coils during the specific experiment with the modulation of LHWs.[25] The HCFs are present in the SOL on the low field side in a DN divertor plasma configuration, with a total number of five, i.e., equal to the number of the LHCD antenna rows.

The resulting stochastic fields at the edge lead to a reduction in the energy ejected during ELM bursts in EAST as with conventional RMPs in other experiments. ELMs can even be completely suppressed with LHCD, without significant degradation of the global plasma confinement. This has been verified by modulating the LHCD power (Fig. 4). The target H-modes produced by ICRH exhibit Type III ELMs with $f_{ELM} \sim 140\,\text{Hz}$, about 10 times Type I ELM frequency in EAST.[17] These ELMs quickly disappear upon fast switching-on of LHCD. What is even more interesting is the emergence of small ELMs with a much higher frequency, i.e., $f_{ELM} \sim 0.5\,\text{kHz}$, which is clearly not Type III ELMs, as the Type III ELM frequency goes down with power, but similar to Type II ELMs.[16] Note that Type I ELMy H-modes have been obtained in EAST with strong ICRH with an ELM frequency of $\sim 10\,\text{Hz}$.[17]

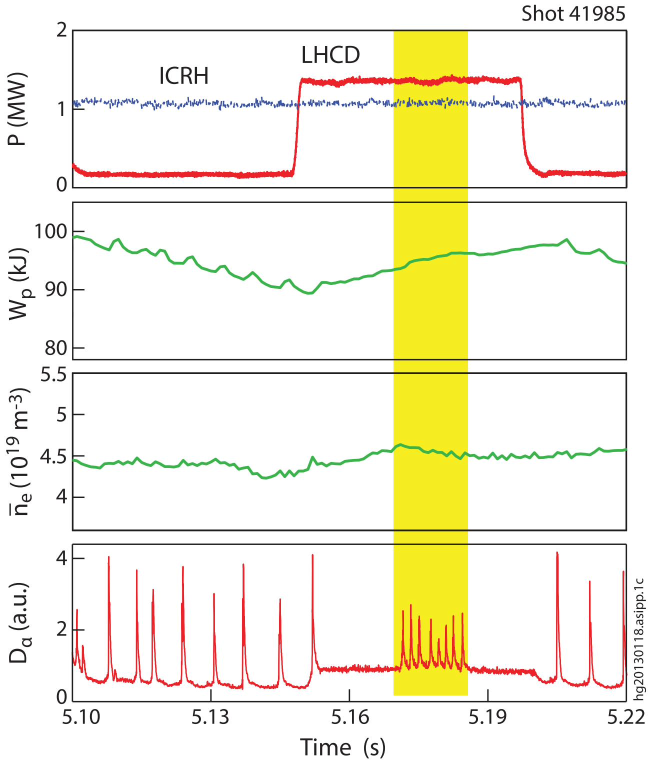

FIG. 4. Demonstration of the effect of LHCD on ELM behavior by modulating LCHD power in a target H-mode plasma produced by ICRH, as manifested by the change in D_α emissions in the outer divertor ($I_p = 500$ KA, $B_T = 2$ T).

In contrast to the widely applied conventional RMP technique with a fixed set of magnetic coils, LHCD intrinsically imposes a flexible boundary control for ELMs over a wide range of plasma currents, or edge safety factor q_{95}.[6] This arises from the natural alignment of LHCD induced magnetic perturbations with resonant magnetic surfaces at the edge, as shown in Fig. 5. The perturbation fields exhibit a helical mode structure with a toroidal mode number $n = 1$, in contrast to the fixed RMP coils, which usually have a toroidal number exceeding unity. Hence, the helicity of the current filaments always closely fits the pitch of the edge field lines for whatever the value of q_{95}, and is thus resonant with the background edge magnetic field created by the current circulating in the plasma. This may have significant implications for effective ELM control in future fusion experiments, such as ITER. Actually, in most of observed cases, ELM control with conventional RMPs created by fixed magnetic coils is usually restricted to a narrow resonant q_{95} window due to the fixed coil geometry.

B. Influence on stationary power deposition

LHCD-RMPs also lead to edge plasma ergodization, which shifts power away from the region near the strike points, thus broadening heat deposition footprints on the divertor target plates, as shown in Fig. 6. The change in the magnetic topology induced by HCFs has been modeled using a field-line-tracing code,[32] by tracing the field lines in the SOL starting in front of the LHW antenna. The traced SOL field lines agree in both position and pitch-angle with the experimentally observed HCF structures. The 3D perturbed magnetic topology and the footprints on the divertor plates can be obtained by superimposing the equilibrium field with the magnetic field induced by the HCFs (Fig. 6). It appears that the structure of the ergodized edge magnetic field has broad regions connecting the divertor target plate at large distances, up to $\sim 20\,\text{cm}$ away from the Outer Strike Point

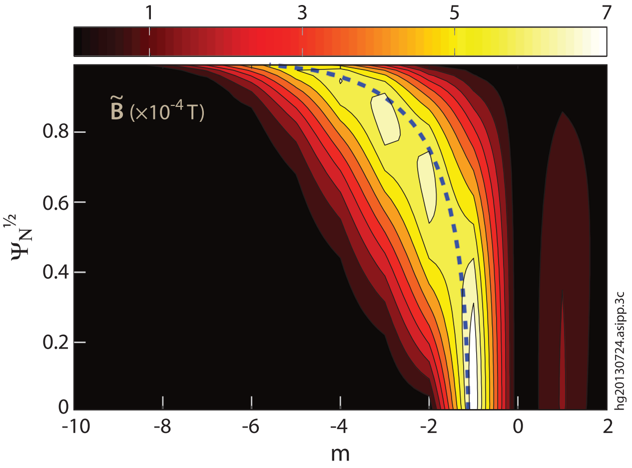

FIG. 5. Contour plot of the magnetic perturbation spectrum showing the Fourier amplitude of the radial component of the toroidal $n = 1$ magnetic field for the H-mode discharge shown in Fig. 4 with $q_{95} = 3.8$, calculated with a total helical filament current of 1.5 kA, uniformly distributed across the current filaments induced by LHCD in the boundary plasma. ψ_N is the normalized poloidal magnetic flux and m is the poloidal mode number. The pitch resonant modes with $m = nq(\psi)$ are shown by the dashed line.

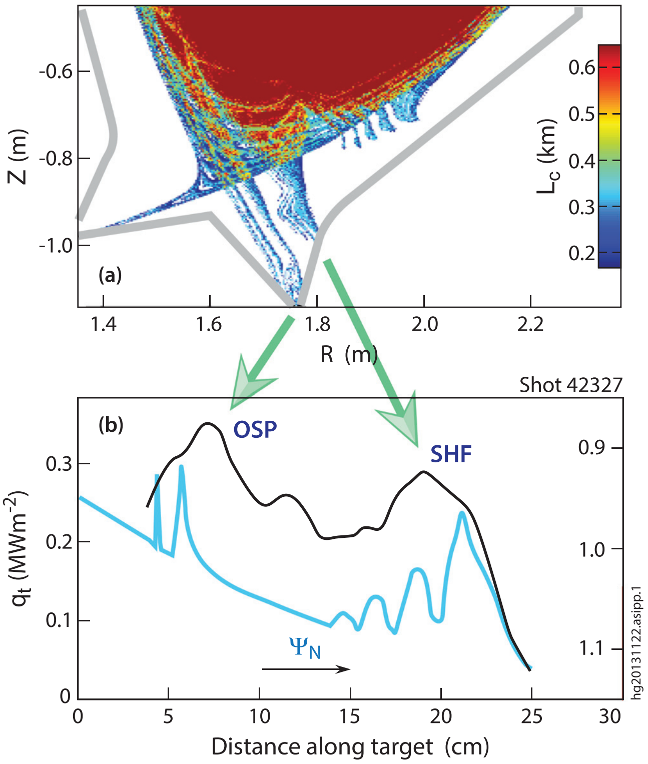

FIG. 6. Demonstration of the influence of edge plasma conditions on the striated heat flux induced by LHCD. (a) The contour of the connection length, L_c, calculated by a field line tracing code with a total LHCD-induced edge current of ∼1.3 kA, determined from the Mirnov probe measurements. (b) Comparison of heat flux profiles at the outer divertor target, obtained from the IR camera, with the predicted penetration depth of the perturbed magnetic fields, as indicated by the normalized poloidal magnetic flux, ψ_N.

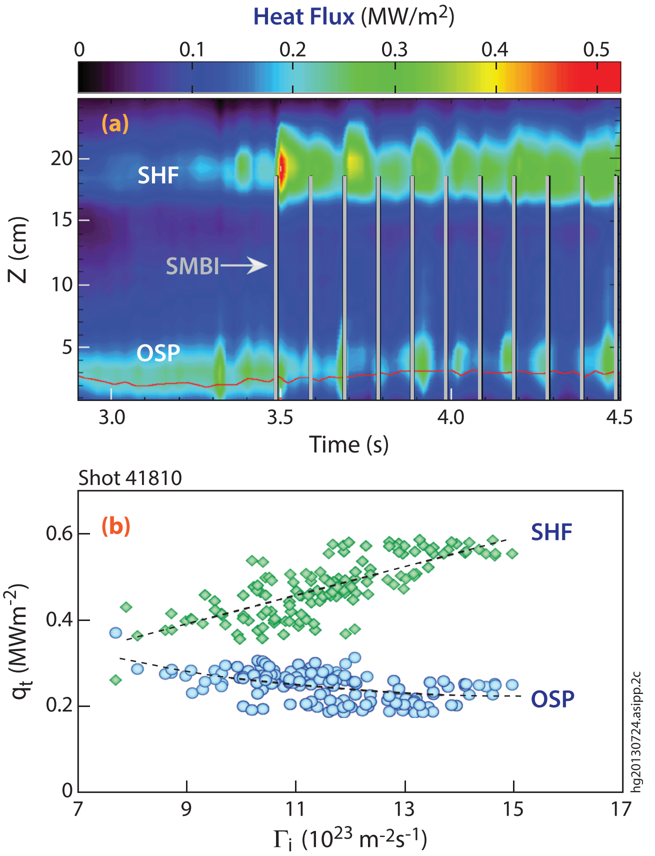

FIG. 7. (a) Contour of divertor heat fluxes on the outer divertor target for a LHCD-driven H-mode discharge with SMBI turned on at 3.5 s. (b) Peak heat flux, q_t, at both SHF and OSP, obtained from the divertor IR camera, as a function of ion flux along the magnetic field line, Γ_i, obtained from the divertor probes.

(OSP). The magnetic perturbations produced by HCFs can extend well inside the separatrix with some flux tubes near the X-point directly intercepted by the outer divertor target plate, thus exhibiting a Striated Heat Flux (SHF) structure, consistent with the experimental observations, as shown in Fig. 6(b).

What is truly remarkable is that the experiments in EAST have demonstrated, for the first time, that the sharing of power deposition between OSP and SHF can be varied by controlling edge plasma conditions, e.g., the divertor ion flux (or edge density), as shown in Fig. 7. Here, the divertor ion flux is regulated by the injection of neutral particles in the plasma with SMBI,[23] under otherwise the same plasma conditions, in terms of plasma current, magnetic field, magnetic configuration, etc. It can be clearly seen in Fig. 7(a) that the application of SMBI reduces the heat fluxes near the OSP region, while further enhancing SHF, thus shifting power deposition from the primary strike point to the SHF in the far SOL region. The ratio of the power deposition at SHF to OSP increases with the SMBI pulse length, i.e., the particle-fuelling rate. This is illustrated in Fig. 7(b) in which the divertor power fluxes at OSP and SHF are plotted versus the divertor ion flux determined by the Langmuir probes. For OSP, increasing the ion flux leads to an initial small decrease and then a nearly constant value of the divertor power flux as expected for a high recycling divertor, $q_{OSP} \sim \Gamma_i \, T_{\text{div}}$, where the divertor temperature T_{div} decreases as the ion flux Γ_i increases, i.e., $T_{div} \sim 1/\Gamma_i$, at constant edge power flow.[33] On the contrary, for SHF, the divertor power flux increases with the ion flux on the field lines directly connecting the divertor to locations in the edge transport barrier with the electron temperature $T_{ped} \sim 350\,\text{eV}$ for typical long-pulse H-mode plasmas in EAST. On these field lines, the divertor electron temperature is expected to be similar to T_{ped} so that $q_{SHF} \sim \Gamma_{SHF} \, T_{ped}$ and thus increases with ion flux as shown in Fig. 7(b). This is a unique physics feature of the ergodized plasma edge obtained in EAST by the application of LHCD, which allows the control of the ratio of q_{SHF}/q_{OSP} and, with it, of the effective divertor power deposition area through the control of the divertor plasma conditions.

Impurity seeding has been adopted as a common technique for stationary heat flux control in present tokamak experiments, which is mandatory for high-power, long-pulse operations, as foreseen for ITER.[2,34] Experiments in EAST with LHCD and Ar seeding to increase divertor radiation and promote divertor detachment have shown a similar phenomenology regarding q_{SHF} to SMBI, as shown in Fig. 8. There is thus potential to combine these two control strategies and provide further benefit, hence, offering an additional actuator for the control of the stationary divertor power load, beyond or in addition to the achievement of conventional highly radiating divertor conditions. This may be of interest for future fusion devices such as ITER, given the small power deposition areas and large associated divertor

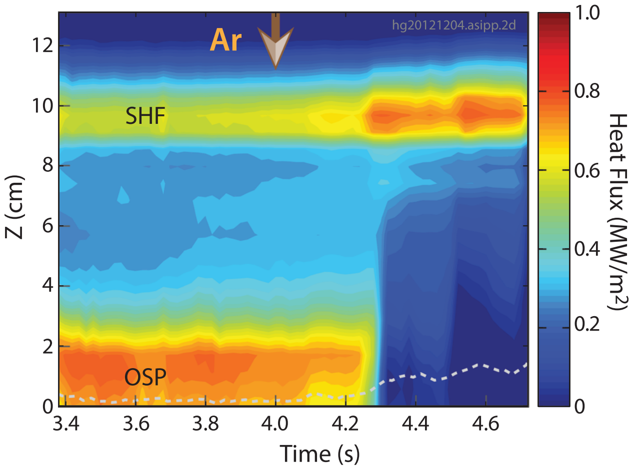

FIG. 8. Contour of divertor heat fluxes on the outer divertor target for a LHCD-driven H-mode discharge showing the effect of Ar puffing on the divertor power deposition between OSP and LHCD-induced SHF.

power fluxes, as expected on the basis of present scalings and physics understanding.[35,36]

V. A NEW EDEGE COHERENT MODE

As mentioned in Sec. III, a new ECM appears in long-pulse H-modes and coexists with small ELMs throughout the H-mode period phase (Fig. 3). This mode has been observed in a broad range of plasma densities with the central-line-averaged density, $\bar{n}_e$, varying from 1.9 to $5 \times 10^{19}\,\mathrm{m}^{-3}$, corresponding to $\bar{n}_e/n_G = 0.28$–0.7, as normalized to the Greenwald density $n_G = I_p/\pi a^2$. The plasma current, I_p, ranges from 0.28 to 0.6 MA in most H-mode discharges. The collisionality evaluated at the top of the pedestal is relatively high, i.e., $\nu_e^* = 0.5$–5, due to relative low heating power available in the last experimental campaign. This mode is present in the steep-gradient pedestal region of the H-mode plasmas with frequency $f_{ECM} = 20$–90 kHz, near the local electron diamagnetic frequency, as detected by the pedestal fluctuation measurements from several edge diagnostics, such as reflectometer, fast moving reciprocating Langmuir probes, and a newly developed dual GPI system (Fig. 2). The mode propagates in the electron diamagnetic drift direction in the plasma frame, as seen by a reciprocating Langmuir probe at the midplane, with a toroidal mode number $n \sim 17$, poloidal wavelength $\lambda_\theta \sim 10\,\mathrm{cm}$ and $k_\theta \rho_s \sim 0.1$, corresponding to a poloidal mode number m over 50.

Note that the ECM is more electrostatic with respect to the QCM (Quasi-Coherent Mode) observed in the Alcator C-mod H-mode plasmas, e.g., see Ref. 37, with a rather weak magnetic perturbation, only about 0.2 Gauss at the mode location, as directly measured by a magnetic pick-up coil installed on the reciprocating probe. The magnetic component of the ECM normalized to the background poloidal field is $\delta B/B_p \sim 1 \times 10^{-4}$, which is much smaller than the QCM in the C-Mod by nearly one order of magnitude. The associated magnetic perturbations can also be detected by fast Mirnov coils located on the low-field side behind the first wall in EAST when the plasma boundary moves close to the coils, but are never seen on the high field side, even though the high-field-side coils are closer to the plasma boundary than those on the low field side are.

This new mode usually starts to appear during pedestal buildup following the L-H transition with an initial frequency chirping down phase of tens of ms, then settling down with a mode frequency at ∼30 kHz, as shown in Fig. 9. ECMs appear to promote particle transport, as evidenced by significantly enhanced Balmer-alpha emissions of deuterium, D_α, in the divertor, which are even higher than those in the L-mode phase, as shown in Fig. 9(a). For this particular shot, the plasma is operated under the LSN configuration with $dR_{sep} = -1.5\,\mathrm{cm}$, the central-line-averaged density $\bar{n}_e \sim 4 \times 10^{19}\,\mathrm{m}^{-3}$ in the H-mode phase, plasma current $I_p = 0.4$ MA, edge safety factor $q_{95} = 4.5$, plasma elongation $\kappa = 1.68$, lower triangularity $\delta_l = 0.44$, and upper triangularity $\delta_u = 0.29$. ECMs coexist with the Type II-like irregular small ELMs, as seen in the long-pulse H-mode shown in Fig. 3. The heat load on the divertor target for such small ELMs is typically less than $2\,\mathrm{MW/m^2}$, as determined by the target embedded Langmuir probes.

Further evidence for continuous particle and heat exhaust across the pedestal, induced by ECMs, is obtained from a multi-purpose fast moving reciprocating probe system at the midplane (Fig. 2). Direct probing inside the separatrix shows that the plasma potential fluctuations appear to lag behind the electron pressure fluctuations by a phase angle of about 10°, and behind the electron density fluctuations by about 20°, hence driving an outward particle and heat flux. As a result, the particle flux driven by ECMs is of the same order of magnitude as the total surface-average particle flux, i.e., $\sim 2 \times 10^{20}\,\mathrm{m}^{-2}\mathrm{s}^{-1}$, while the total heat exhaust by this mode is ∼0.2–0.4 MW, which is about 15%–30% of the total loss power through the plasma boundary, for a typical

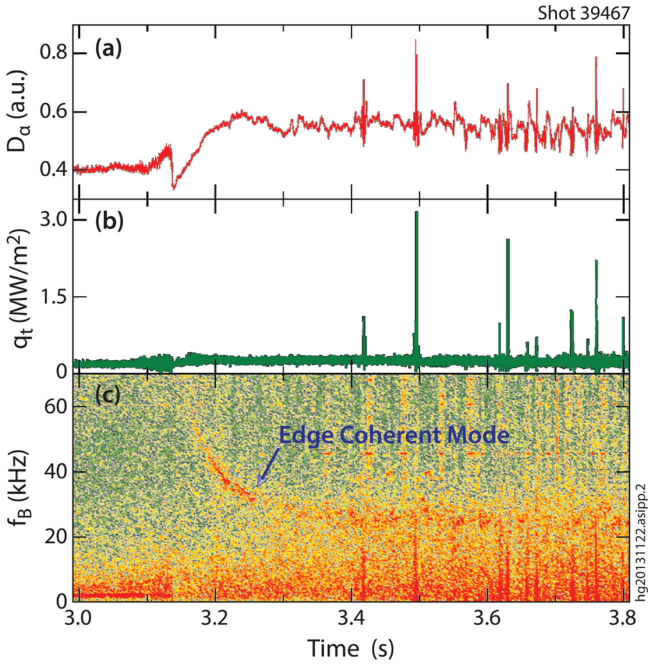

FIG. 9. (a) Divertor D_α emission and (b) heat load on the lower outer divertor target, evaluated from the target embedded Langmuir probe measurements. (c) Power spectrum of magnetic fields measured by a fast Mirnov probe located on the low-field side behind the first wall.

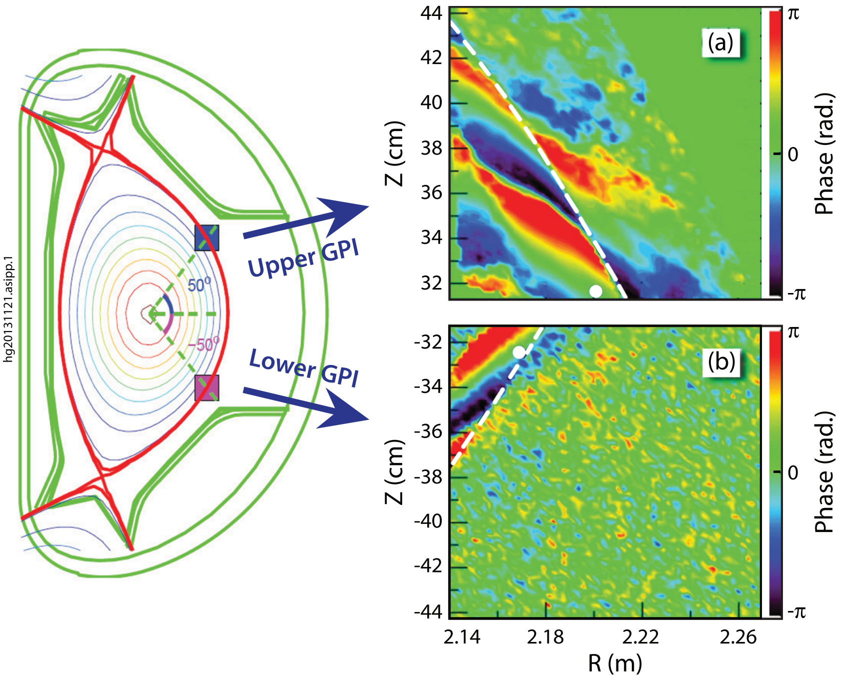

FIG. 10. Cross phase imaging from (a) the upper view area and (b) the lower view area in the ECM frequency range with respect to a reference pixel marked by a solid white circle. The dashed line indicates the location of the separatrix.

H-mode plasma. The electrostatic component of the ECM is rather strong, with a relative fluctuation level in the plasma potential and the electron pressure of ~0.4.

Detailed mode structure has been obtained from the dual GPI system, which is located on the low-field side with two 13 × 13 cm square view areas at the edge, symmetrically about the midplane and toroidally separated by 66.6°.[38] With the injection of Helium (He), the edge fluctuations are imaged by viewing He I line emission at 587.6 nm through two telescopes along the local magnetic field lines at the different poloidal locations. The images are recorded simultaneously by two fast cameras at a frame rate of 391 kHz and a resolution of 64 × 64 pixels with a 12-bit dynamic range. The mode peaks at about 1 cm inside the separatrix with a radial spread of about 1 cm. ECM exhibits a nearly up-down symmetric tilted structures, with the tilting angles in the opposite directions in the upper and lower imaging regions, as shown in Fig. 10. This is possibly induced by the magnetic shear, since the flow shear would tilt the structures in the same direction. Based on the cross phase patterns for the two poloidally separated GPI views, the poloidal wavelength of the ECM is estimated to be $\lambda_\theta \sim 10$ cm, consistent with the Langmuir probe measurements.

Simulations using GYRO's eigenvalue solver[39] have been performed in a flux tube domain near the peak gradient pedestal region with realistic geometry from kinetic EFIT[40] and full gyrokinetic species, taking into account electromagnetic effects, collisions and plasma rotation. The GYRO simulations show a mode in the steep-gradient pedestal region, exhibiting the nature of dissipative trapped electron mode (DTEM). The mode propagates in the electron diamagnetic direction at a frequency near the local electron diamagnetic frequency, consistent with the characteristics of the experimentally observed ECM. Furthermore, the growth rate of this mode peaks in the same $k_\theta \rho_s$ range as the experimental observations, decreasing towards the high k region. Figure 11 shows the collisionality scan with $k_\theta \rho_s$ fixed at 0.1. The mode appears to be unstable in the same range of collisionalities as in the experiments, peaking at $\nu_e^* = 2.2$, which is destabilized by the enhanced local T_e gradient, but not sensitive to T_i and n_e gradients or β, as expected for the DTEM. In addition, the modeling shows that the amplitude of the magnetic component is about 30 times smaller than the electrostatic component, implying that it is a predominantly electrostatic mode, again in agreement with the experimental observations.

VI. EFFECT OF MAGNETIC CONFIGURATIONS

The preferred scenario for achieving long-pulse H-modes in EAST was to operate with reversed toroidal field, i.e., with the ion ∇B drift towards the upper divertor.[8] This induces a preferential plasma flow towards the bottom, thus facilitating particle exhaust by divertor pumping

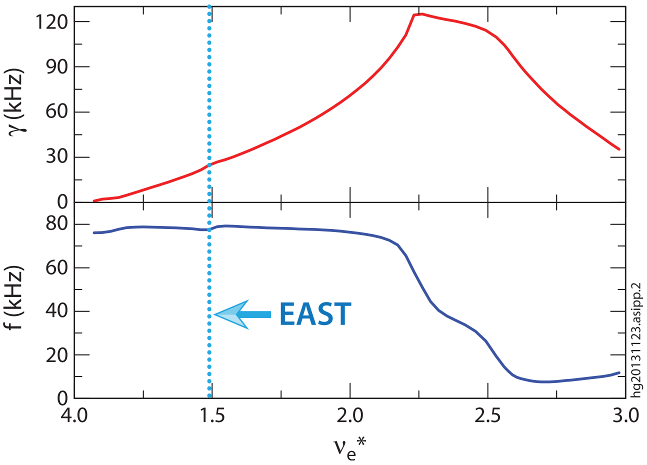

FIG. 11. (a) Growth rate and (b) real frequency versus normalized collisionality ν_e^* of the most unstable mode in the peak gradient pedestal region, predicted by the GYRO code.

available from the bottom divertor. Figure 12 shows the contours of the ion saturation current density measured by the Langmuir probes, j_s, at the upper outer (UO) and lower outer (LO) divertor targets for two ELMy H- mode discharges obtained under the DN divertor configuration with the ion ∇B drift towards the top and bottom divertors, respectively. As can be seen, with the ion ∇B drift towards the bottom divertor ($\mathbf{B} \times \nabla B \downarrow$), more particle fluxes from ELMs go to the upper divertor target, i.e., in the *opposite* direction to the ion ∇B drift, as indicated by the contours of ion saturation current density, j_s. This trend is completely reversed as the ion ∇B drift direction is reversed, i.e., towards the top divertor ($\mathbf{B} \times \nabla B \uparrow$), with most of particle fluxes reaching the bottom divertor target. This is most likely due to classical drifts, as such an up-down asymmetry observed in the DN divertor configuration does not involve geometric effects,[41] in contrast to SN.

Furthermore, contrary to expectations, access to H-modes in EAST with LHCD alone or combined with ICRH exhibits a lower power threshold with the ion ∇B drift directed away from the active divertor. Actually, Type I ELMy H-modes has so far been achieved in EAST only in LSN for reversed B_T,[7] with the limited heating power presently available. This, along with the ease of particle exhaust with divertor pumping at the bottom, may explain the "unusual" EAST preferred operation scheme, which favors *reversed* B_T.

To better understand ELM dynamics and footprints on the divertor targets in EAST, modeling has been carried out using the BOUT++ code package. BOUT++ is a framework for performing plasma simulations in curvilinear geometry, incorporating the two-fluid[42,43] and Gyro-Landau-Fluid models[44] to simulate the dynamics of ELMs in real tokamak geometries.[45] In addition, the six-field two-fluid module is developed to study the properties of the turbulence, transport, and heat flux during ELMy H-mode discharges.[43] The input parameters for the simulation are taken from an LHCD-driven H-mode discharge (#38300), under a near DN divertor configuration with $dRsep = -0.8$ cm, i.e., close to the LSN, with the ion ∇B drift towards the bottom (normal B_T). Here, $dR_{sep} = R_{sep,L} – R_{sep,U}$, with $R_{sep,L}$ and $R_{sep,U}$ being the lower and upper separatrix radii mapped to the outer midplane. The measured density and temperatures are used as the input H-mode profiles inside the separatrix, while the profiles outside the separatrix are assumed constant. The electric field is calculated with the assumption of zero net zonal flow, i.e., the equilibrium zonal flow is balanced with the ion diamagnetic flow. In addition, the nonlinear Spitzer resistivity is used in the simulation. Because the spatial distribution of fast changes in plasma density and temperature profiles in the edge pedestal across the separatrix, the nonlinear flux-limited expression is adopted for parallel thermal diffusivities in a harmonic average, as described in Ref. 43.

Figure 13 shows the evolution of the poloidal structure during an ELM event, predicted by BOUT++, in the following different phases. (a) *Linear growing*: The fluctuations grow up linearly, dominated by the $n = 5$ mode. (b) *Saturation*: The system enters the nonlinear phase, manifested by the turbulence. (c) *ELM filament formation*: The filaments (shown in red) formed again with a dominant $n = 5$ mode structure, as in the linear phase. The filaments move outward and finally eject outside the separatrix. Figure 14 shows the particle fluxes on the UO and LO divertor targets during the ELM crash, calculated by BOUT++. Clearly, the particle flux at the top divertor is much larger than that at the bottom, with the peak amplitude of ~60 A/cm^2, in agreement with the divertor probe measurements, as shown in Fig. 12, for the discharge with the ion ∇B drift towards the bottom. The direction of the particle flow is opposite to the poloidal $\mathbf{E} \times \mathbf{B}$ and ion ∇B drift, in the same direction as the

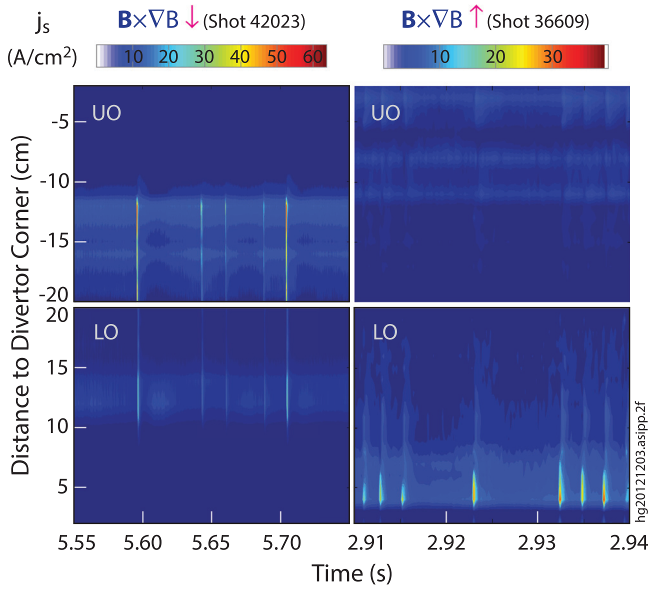

FIG. 12. Contours of j_s at the upper and lower outer divertor targets for two ELMy H-mode discharges obtained under the DN divertor configuration, with the ion ∇B drift toward the bottom ($\mathbf{B} \times \nabla B \downarrow$) and top ($\mathbf{B} \times \nabla B \uparrow$) divertors, respectively. The ELMs are manifested by the colorful stripes on the blue background of the j_s contour plots.

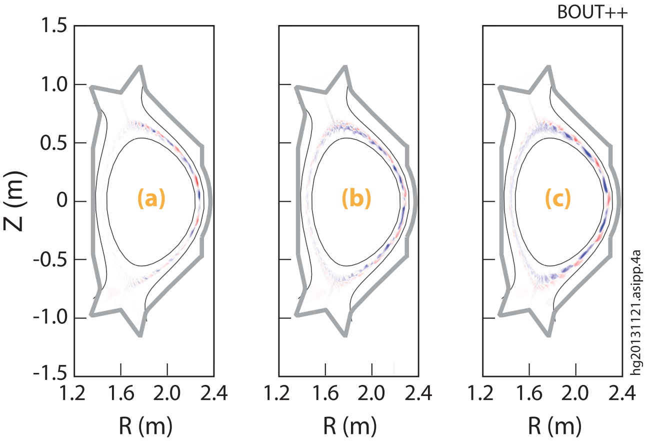

FIG. 13. The evolution of the poloidal mode structure during an ELM crash event for a typical H-mode discharge (#38300) in EAST. (a) Linear phase before the ELM event (t = 0.06 ms). (b) Saturation phase (t = 0.08 ms) during which turbulence becomes dominant. (c) ELM burst (t = 0.1 ms), showing an obvious filamentary structure with the filaments moving radially outwards. Positive fluctuations (blobs) shown in red, and negative perturbations (holes) in blue.

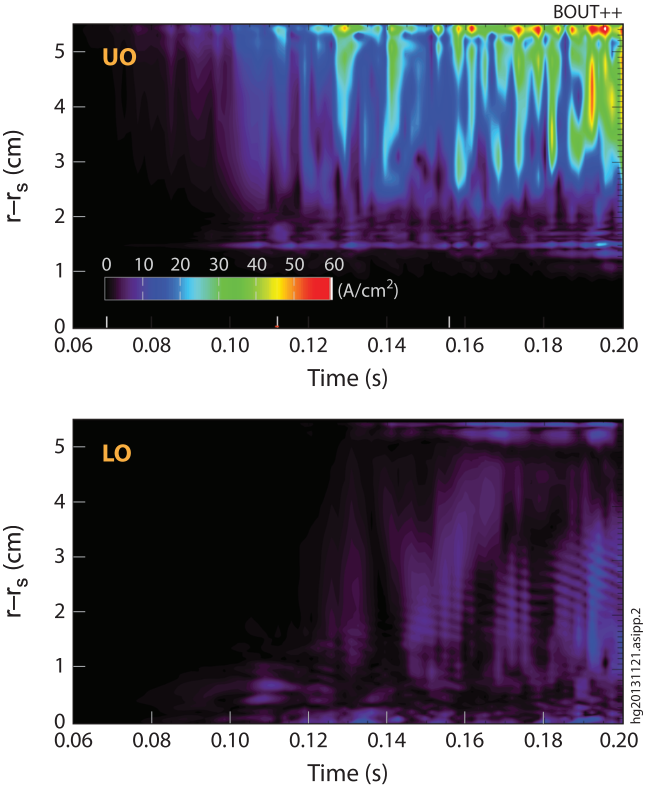

FIG. 14. Particle fluxes on the UO and LO divertor targets during an ELM crash, computed by BOUT++, for a typical H-mode discharge in EAST under a near DN divertor configuration with the ion ∇B drift towards the bottom, showing a clear up-down asymmetry, favoring the top divertor, consistent with experimental observations.

Pfirsch-Schlüter flow, as observed experimentally. This is very interesting and awaits further investigations.

VII. DEVELOPMENT OF ADVANCED TOKAMAK SCENARIOS FOR EAST

A. First results from joint experiments in DIII-D

In order to develop and test a possible scenario for steady-state advanced tokamak demonstration on EAST, an experiment was designed and carried out on the DIII-D tokamak at General Atomics in San Diego, USA. The experiment demonstrated that fully noninductive H-mode plasma operation is possible with plasma parameters and plasma formation consistent with capabilities expected for EAST after the recent upgrades.

Building on earlier DIII-D work,[46] the experiment utilized an approach to fully noninductive operation based on very high bootstrap fraction. Figure 15 shows time histories of several plasma parameters for a representative discharge. The plasma cross section is an upper biased double null divertor shape, with elongation $\kappa \sim 1.86$ and average triangularity (top and bottom) ∼0.6, a shape that EAST can reproduce. The toroidal field is $B_T = 2$ T. The plasma current ramp up rate is limited to 0.25 MA/s, consistent with EAST constraints. After an approximate equilibrium is established (1.7 s), the current in the transformer coil is fixed so that the plasma current is forced to relax noninductively. A flat-top at approximately 0.6 MA is maintained by increasing β_N and thus the bootstrap current fraction, until a 100% noninductive condition is achieved and maintained for the rest of the discharge duration, limited by hardware constraints on DIII-D pulse length. The discharge achieves and maintains $\beta_N \sim \beta_P \geq 3\%$ and $\beta_T \sim 1.5\%$ using total heating and current drive power of ∼11 MW. This power includes ∼5 MW of off-axis Neutral Beam Injection (NBI) ($\rho \sim 0.4$), and 2.5 MW of off-axis Electron Cyclotron Current Drive, ECCD ($\rho = r/a \sim 0.5$), intended to simulate as close as possible the off-axis current drive from LHW on EAST. The various current components plotted in Fig. 16(c) are calculated from experimental profiles by the TRANSP code.[47] The bootstrap current fraction reaches up to 75%–80%, the NBI-driven current fraction is 15%–20%, and only <5% of the total current is driven by electron cyclotron frequency

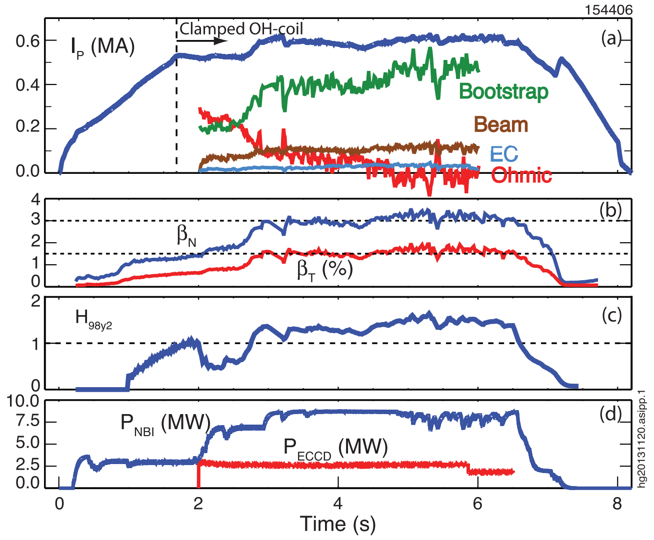

FIG. 15. Demonstration of a fully noninductive H-mode plasma achieved in DIII-D with plasma parameters and plasma formation consistent with capabilities expected for EAST in 2014.

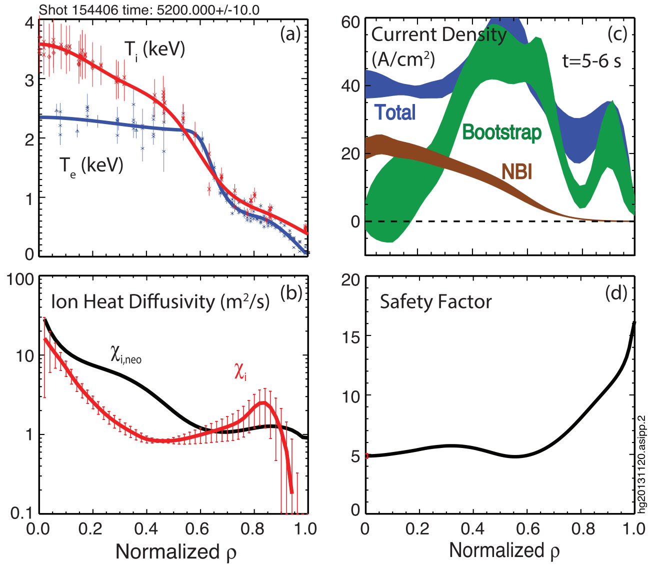

FIG. 16. Radial profiles for the shot shown in Fig. 15. (a) Representative radial profiles for T_e and T_i. (b) Ion heat diffusivity, χ_i, calculated by TRANSP and the expected neoclassical values, $\chi_{i,neo}$. (c) Current density profiles for the various current components, and (d) safety factor, q.

electromagnetic waves, since the efficiency of ECCD is very low at large minor radius.

This plasma exhibits excellent energy confinement quality with confinement enhancement factor over H-mode confinement scaling $H_{98(y,2)} \sim 1.5$. Similar confinement was also obtained at reduced NBI torque, matching the NBI torque ~3 Nm expected on EAST. This excellent confinement is associated with the formation of an internal transport barrier (ITB) at large minor radius ($\rho > 0.5$) in all channels (n_e, T_e, T_i, rotation). Fig. 16(a) shows representative radial profiles for T_e and T_i, both exhibiting a large gradient at $\rho \sim 0.7$. In Fig. 16(b), the ion heat diffusivity calculated by TRANSP is shown to drop below the neoclassical predicted levels at $\rho \sim 0.7$, indicating strong reduction of transport and confirming the presence of an ITB. Fig. 16(c) shows a very broad bootstrap current profile that is fairly well-aligned with the total current profile, explaining why the minimum safety factor is high [Fig. 16(d)] and constant or slowly increasing, and the ITB is maintained at $\rho > 0.5$ for ~4 s, more than three times the current relaxation time, estimated to be ~1 s. These DIII-D results build the foundation for follow-up experiments to be conducted on EAST, where the superconducting coils enable extension to very long pulse, and verification of compatibility of this regime with reactor relevant boundary conditions.

B. Predictions for EAST advanced scenarios

Modeling has been carried out to explore the advanced scenarios on EAST by PTRANSP code in combination with TSC,[48,49] using the DIII-D experimental results as guidance and taking into account the EAST capabilities expected for the next experimental campaign in 2014. The modules involved in simulations include TEQ for magnetic equilibrium, CDBM for plasma transport, NUBEAM for neutral beam injection, LSC for LHW current drive, TORIC for ion cyclotron resonance heating/current drive, and TORAY for electron cyclotron resonance heating/current drive.[50–56]

Simulations show that such DIII-D scenarios are accessible on EAST for a steady-state plasma with $I_p = 0.5$ MA, $n_e/n_G = 0.7$, and $B_T = 2.5$ T by utilizing half of the total EAST H&CD capabilities expected for 2014. Fig. 17(a) shows the heating and current drive scheme adopted in the simulation. A short NBI pulse, up to 4 MW, is applied during the current ramp-up phase as preheating to produce a hot target plasma. Then, the major RF power is applied during the current flattop phase, with a dominant ICRH power of 6 MW in the NBI preheated target plasma. The modeling shows that $\beta_N \sim 3.0$ and $H_{98(y,2)} \sim 1.6$ can be achieved using this heating scheme. The fully non-inductive plasma state is achieved at 4.2 s, with the bootstrap current fraction as high as 80% (~0.4 MA), as shown in Fig. 17(b). The q profile and current density profiles at 4.6 s are shown in Fig. 17(c) and Fig. 17(d), respectively. As can be seen, the q profile is largely flat in the plasma core region, except for a slight bump around $\rho \sim 0.35$, exhibiting a low core magnetic shear with $q_{max} - q_{min} < 1$ within $\rho < 0.75$.

In addition, the modelling also demonstrates potential steady-state operations at 0.8 MA with a bootstrap fraction up to 70% for EAST. As in the scenario developed for 0.5 MA, NBI is only applied during the initial plasma current ramp-up phase for pre-heating. The high performance plasma is fully sustained by ICRF and LHW power and features a weak core magnetic shear with an ITB footprint at $\rho \sim 0.6$, similar to the scenarios demonstrated in DIII-D. It can be extended over a time scale much longer than the resistive diffusion time with the expected operational capabilities in the forthcoming EAST experimental campaign.

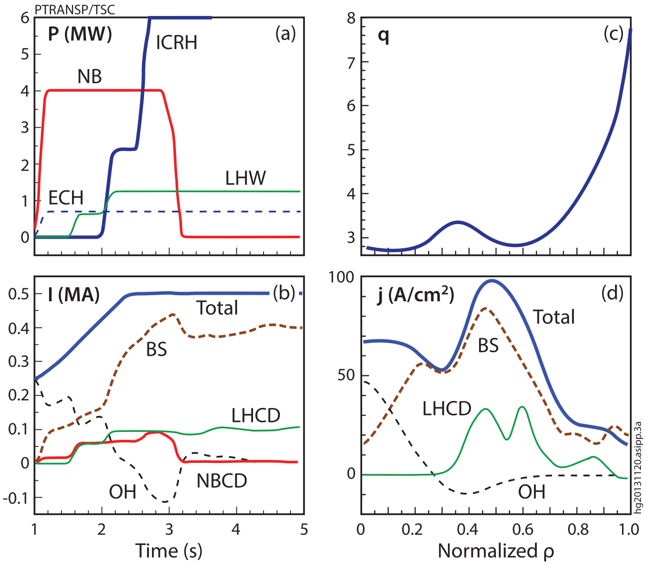

FIG. 17. Simulations of a steady-state advanced tokamak scenario for EAST, based on the DIII-D experimental results. (a) Waveforms of input auxiliary power, which is compatible with the heating and current drive capability in the EAST in 2014. (b) Evolution of different current channels. (3) Predicted q profile at 4.6 s. (4) Predicted current density profiles at 4.6 s.

VIII. SUMMARY AND CONCLUSIONS

Significant progress has been made in EAST on both technology and physics fronts towards high-power, long-pulse operations, achieving reproducible high-confinement H-mode plasmas over 30 s, which exhibit a Type II-like small ELMs with a confinement quality between Type I and Type III ELMy H-modes, i.e., $H_{98(y,2)} \sim 0.9$ and peak heat fluxes largely below 2 MW/m^2. This long-pulse H-mode regime is obtained with extensive lithium wall conditioning and predominant heating and current drive from LHCD. LHCD also drives currents in SOL, leading to a 3D distortion of the magnetic topology at the edge, hence changing the ELM pattern, similar to the conventional RMPs. What is even more remarkable is that LHCD imposes intrinsically a flexible boundary control for ELMs due to the alignment of LHCD induced magnetic perturbations with resonant magnetic surfaces at the edge. Furthermore, LHCD-RMPs have a positive effect on the control of stationary power load by broadening heat deposition footprints on the divertor targets; the heat transport caused by plasma ergodization can be actively controlled by changing edge plasma density, e.g., with SMBI or gas puffing. Note that the high q and strong collisionality in EAST might have enhanced the LHCD effect. Another interesting finding is that a continuous MHD mode localized at the edge, i.e., ECM, coexists with small

ELMs throughout the long-pulse H-mode, enhancing outward radial particle and power transport.

In addition, the magnetic configuration exhibits a strong influence on long-pulse operations. It appears that ELMs induce a significant up-down asymmetry with preferential plasma flow in the direction opposite to the ion ∇B drift, i.e., with a larger particle flux at the upper divertor target for normal B_T, which has been quantitatively reproduced by the BOUT++ code package. This trend is completely reversed with more particles moving to the lower divertor as B_T is reversed, thus facilitating particle exhaust, because divertor pumping is available at the bottom. This, coupled with a lower power threshold required for the L-H transition when the ion ∇B drift is away from the active divertor in EAST, makes reversed B_T a preferred scenario for long-pulse operations.

EAST is now undertaking an extensive upgrade with enhanced current drive and heating capabilities, with a total power exceeding 20 MW. The upper divertor is upgraded to the ITER-like W monoblock target structure with flat-type domes to allow for high heat load on divertor targets, up to 10 MW/m^2. The second in-vessel cryopump is installed in the upper divertor behind the outer target to improve particle exhaust. In addition, an RMP system with 2 (poloidal) × 8 (toroidal) coils will be implemented, along with many new or upgraded diagnostics. Recently, a steady-state advanced tokamak operation scenario has been developed for EAST in collaboration with General Atomics. The initial test on DIII-D has demonstrated that fully noninductive H-mode plasma operation is possible with plasma parameters and plasma formation schemes consistent with capabilities expected for EAST in 2014. These will enable EAST to address some critical issues facing high-power, long-pulse plasma operations in the near future.

ACKNOWLEDGMENTS

We would like to acknowledge the support and contributions from the rest of the EAST team and collaborators. This work was supported in part by National Magnetic Confinement Fusion Science Program of China under Contract Nos. 2010GB104001, 2010GB104002, 2011GB101000, 2011GB107001, 2012GB101001, 2013GB107003, and 2013GB106003, National Nature Science Foundation of China under Contract Nos. 11021565, 10725523, 10990212, JSPS-NRF-NSFC A3 Foresight Program in the field of Plasma Physics (NSFC No. 11261140328), and Magnetic Confinement Innovation Team Plan of Chinese Academy of Sciences (No. 11321092), as well as the Thousand Talent Plan of China and Helmholtz Association in the frame of the Helmholtz-University Young Investors Group VH-NG-410. The views and opinions expressed herein do not necessarily reflect those of the ITER Organization.

[1] E. Tsitrone, J. Nucl. Mater. **363–365**, 12 (2007).

[2] A. Loarte, B. Lipschultz, A. S. Kukushkin, G. F. Matthews, P. C. Stangeby, N. Asakura, G. F. Counsell, G. Federici, A. Kallenbach, K. Krieger, A. Mahdavi, V. Philipps, D. Reiter, J. Roth, J. Strachan, D. Whyte, R. Doerner, T. Eich, W. Fundamenski, A. Herrmann, M. Fenstermacher, P. Ghendrih, M. Groth, A. Kirschner, S. Konoshima, B. LaBombard, P. Lang, A. W. Leonard, P. Monier-Garbet, R. Neu, H. Pacher, B. Pegourie, R. A. Pitts, S. Takamura, J. Terry, E. Tsitrone, and ITPA Scrape-off Layer and Divertor Physics Topical Group, "Progress in the ITER physics basis - Chapter 4: Power and particle control," Nucl. Fusion **47**, S203 (2007).

[3] P. C. Stangeby, *The Plasma Boundary of Magnetic Fusion Devices* (IOP, Bristol, 2000).

[4] Y. Wan, Nucl. Fusion **40**, 1057 (2000).

[5] F. Wagner, G. Becker, K. Behringer, D. Campbell, A. Eberhagen, W. Engelhardt, G. Fussmann, O. Gehre, J. Gernhardt, G. v. Gierke, G. Haas, M. Huang, F. Karger, M. Keilhacker, O. Klüber, M. Kornherr, K. Lackner, G. Lisitano, G. G. Lister, H. M. Mayer, D. Meisel, E. R. MIiller, H. Murmann, H. Niedermeyer, W. Poschenrieder, H. Rapp, H. Röhr, F. Schneider, G. Siller, E. Speth, A. Stäbler, K. H. Steuer, G. Venus, O. Vollmer, and Z. Yü, Phys. Rev. Lett. **49**, 1408 (1982).

[6] J. Li, H. Y. Guo, B. N. Wan, X. Z. Gong, Y. F. Liang, G. S. Xu, K. F. Gan, J. S. Hu, H. Q. Wang, L. Wang, L. Zeng, Y. P. Zhao, P. Denner, G. L. Jackson, A. Loarte, R. Maingi, J. E. Menard, M. Rack, and X. L. Zou, Nat. Phys. **9**, 817 (2013).

[7] B. Wan, J. Li, H. Guo, Y. Liang, G. Xu, and X. Gong for EAST Team and International Collaborators, Nucl. Fusion **53**, 104006 (2013).

[8] H. Y. Guo, J. Li, X. Z. Gong, B. N. Wan, J. S. Hu, L. Wang, H. Q. Wang, J. E. Menard, M. A. Jaworski, K. F. Gan, S. C. Liu, G. S. Xu, S. Y. Ding, L. Q. Hu, Y. F. Liang, J. B. Liu, G. N. Luo, H. Si, D. S. Wang, Z. W. Wu, L. Y. Xiang, B. J. Xiao, L. Zhang, X. L. Zou, D. L. Hillis, A. Loarte, R. Maingi, and EAST Team, Nucl. Fusion **54**, 013002 (2014).

[9] W. Morris, "Fusion's Eastern promise?," Nat. Phys. **9**, 754 (2013).

[10] G. Z. Zuo, J. S. Hu, S. Zhen, J. G. Li, D. K. Mansfield, B. Cao, J. H. Wu, L. E. Zakharov, and EAST Team, Plasma Phys. Controlled Fusion **54**, 015014 (2012).

[11] D. K. Mansfield, A. L. Roquemore, H. Schneider, J. Timberlake, H. Kugel, M. G. Bell, and NSTX Research Team, Fusion Eng. Des. **85**, 890–895 (2010).

[12] B. J. Xiao, D. A. Humphreys, M. L. Walker, A. Hyatt, J. A. Leuer, D. Mueller, B. G. Penaflor, D. A. Pigrowski, R. D. Johnson, A. Welander, Q. P. Yuan, H. Z. Wang, J. R. Luo, Z. P. Luo, C. Y. Liu, L. Z. Liu, and K. Zhang, Fusion Eng. Des. **83**, 181 (2008).

[13] G. S. Xu, B. N. Wan, J. G. Li, X. Z. Gong, J. S. Hu, J. F. Shan, H. Li, D. K. Mansfield, D. A. Humphreys, and V. Naulin for EAST Team and International Collaborators, Nucl. Fusion **51**, 072001 (2011).

[14] D. N. Hill, J. Nucl. Mater. **241–243**, 182 (1997).

[15] M. Shimada, D. J. Campbell, V. Mukhovatov, M. Fujiwara, N. Kirneva, K. Lackner, M. Nagami, V. D. Pustovitov, N. Uckan, J. Wesley, N. Asakura, A. E. Costley, A. J. H. Donné, E. J. Doyle, A. Fasoli, C. Gormezano, Y. Gribov, O. Gruber, T. C. Hender, W. Houlberg, S. Ide, Y. Kamada, A. Leonard, B. Lipschultz, A. Loarte, K. Miyamoto, V. Mukhovatov, T. H. Osborne, A. Polevoi, and A. C. C. Sips, "Progress in the ITER physics basis - Chapter 1: Overview and summary," Nucl. Fusion **47**, S1 (2007).

[16] E. J. Doyle, W. A. Houlberg, Y. Kamada, V. Mukhovatov, T. H. Osborne, A. Polevoi, G. Bateman, J. W. Connor, J. G. Cordey, T. Fujita, X. Garbet, T. S. Hahm, L. D. Horton, A. E. Hubbard, F. Imbeaux, F. Jenko, J. E. Kinsey, Y. Kishimoto, J. Li, T. C. Luce, Y. Martin, M. Ossipenko, V. Parail, A. Peeters, T. L. Rhodes, J. E. Rice, C. M. Roach, V. Rozhansky, F. Ryter, G. Saibene, R. Sartori, A. C. C. Sips, J. A. Snipes, M. Sugihara, E. J. Synakowski, H. Takenaga, T. Takizuka, K. Thomsen, M. R. Wade, H. R. Wilson, ITPA Transport Physics Topical Group, ITPA Confinement Database and Modelling Topical Group, and ITPA Pedestal and Edge Topical Group, "Progress in the ITER physics basis - Chapter 2: Plasma confinement and transport," Nucl. Fusion **47**, S18 (2007).

[17] L. Wang, G. S. Xu, H. Y. Guo, H. Q. Wang, S. C. Liu, K. F. Gan, X. Z. Gong, Y. Liang, N. Yan, L. Chen, J. B. Liu, W. Zhang, R. Chen, L. M. Shao, H. Xiong, J. P. Qian, B. Shen, G. J. Liu, R. Ding, X. J. Zhang, C. M. Qin, S. Ding, L. Y. Xiang, G. H. Hu, Z. W. Wu, G. N. Luo, J. L. Chen, L. Q. Hu, X. Gao, B. N. Wan, J. G. Li, and EAST Team, Nucl. Fusion **53**, 073028 (2013).

[18] T. Ozeki, M. S. Chu, L. L. Lao, T. S. Taylor, M. S. Chance, S. Kinoshita, K. H. Burrell, and R. D. Stambaugh, Nucl. Fusion **30**, 1425 (1990).

[19] J. Stober, M. Maraschek, G. D. Conway, O. Gruber, A. Herrmann, A. C. C. Sips, W. Treutterer, H. Zohm, and ASDEX Upgrade Team, Nucl. Fusion **41**, 1123 (2001).

[20] A. C. C. Sips, R. Arslanbekov, C. Atanasiu, W. Becker, G. Becker, K. Behler, K. Behringer, A. Bergmann, R. Bilato, D. Bolshukhin, K. Borrass,

B. Braams, M. Brambilla, F. Braun, A. Buhler, G. Conway, D. Coster, R. Drube, R. Dux, S. Egorov, T. Eich, K. Engelhardt, H.-U. Fahrbach, U. Fantz, H. Faugel, M. Foley, K. B. Fournier, P. Franzen, J. C. Fuchs, J. Gafert, G. Gantenbein, O. Gehre, A. Geier, J. Gernhardt, O. Gruber, A. Gude, S. Günter, G. Haas, D. Hartmann, B. Heger, B. Heinemann, A. Herrmann, J. Hobirk, F. Hofmeister, H. Hohenöcker, L. Horton, V. Igochine, D. Jacobi, M. Jakobi, F. Jenko, A. Kallenbach, O. Kardaun, M. Kaufmann, A. Keller, A. Kendl, J.-W. Kim, K. Kirov, R. Kochergov, H. Kollotzek, W. Kraus, K. Krieger, B. Kurzan, P. T. Lang, P. Lauber, M. Laux, F. Leuterer, A. Lohs, A. Lorenz, C. Maggi, H. Maier, K. Mank, M.-E. Manso, M. Maraschek, K. F. Mast, P. McCarthy, D. Meisel, H. Meister, F. Meo, R. Merkel, D. Merkl, V. Mertens, F. Monaco, A. Mück, H. W. Müller, M. Münich, H. Murmann, Y.-S. Na, G. Neu, R. Neu, J. Neuhauser, J.-M. Noterdaeme, I. Nunes, G. Pautasso, A. G. Peeters, G. Pereverzev, S. Pinches, E. Poli, M. Proschek, R. Pugno, E. Quigley, G. Raupp, T. Ribeiro, R. Riedl, S. Riondato, V. Rohde, J. Roth, F. Ryter, S. Saarelma, W. Sandmann, S. Schade, H.-B. Schilling, W. Schneider, G. Schramm, S. Schweizer, B. Scott, U. Seidel, F. Serra, S. Sesnic, C. Sihler, A. Silva, E. Speth, A. Stäbler, K.-H. Steuer, J. Stober, B. Streibl, E. Strumberger, W. Suttrop, A. Tabasso, A. Tanga, G. Tardini, C. Tichmann, W. Treutterer, M. Troppmann, P. Varela, O. Vollmer, D. Wagner, U. Wenzel, F. Wesner, R. Wolf, E. Wolfrum, E. Würsching, Q. Yu, D. Zasche, T. Zehetbauer, H.-P. Zehrfeld, and H. Zohm, Plasma Phys. Controlled Fusion **44**, B69 (2002).

[21] G. Saibene, R. Sartori, A. Loarte, D. J. Campbell, P. J. Lomas, V. Parail, K. D. Zastrow, Y. Andrew, S. Sharapov, A. Korotkov, M. Becoulet, G. T. A. Huysmans, H. R. Koslowski, R. Budny, G. D. Conway, J. Stober, W. Suttrop, A. Kallenbach, M. von Hellermann, and M. Beurskens, Plasma Phys. Controlled Fusion **44**, 1769 (2002).

[22] R. Maingi, A. E. Hubbard, H. Meyer, J. W. Hughes, A. Kirk, R. Maqueda, J. L. Terry, and Alcator C-Mod, MAST, and NSTX Teams, Nucl. Fusion **51**, 063036 (2011).

[23] X. L. Zou, X. Z. Gong, J. S. Hu, H. Y. Guo, L. Q. Hu, J. G. Li, B. N. Wan, W. W. Xiao, P. H. Diamond, Y. F. Liang, G. S. Xu, J. H. Li, K. F. Gan, L. Wang, S. B. Zhang, A. D. Liu, J. P. Qian, B. Shen, S. Y. Lin, A. Ti, X. W. Zheng, F. K. Liu, J. F. Shan, B. J. Ding, M. Wang, Y. P. Zhao, X. J. Zhang, C. M. Qin, X. H. Zhang, W. Gao, L. Zhang, T. H. Shi, T. Zhang, Y. M. Wang, Y. X. Jie, LQ. Xu, J. Z. Zhang, Y. M. Duan, B. Lu, F. D. Wang, Y. Y. Li, and EAST Team, in *Proceedings of the 24th IAEA Fusion Energy Conference, October 8–13, San Diego (IAEA, 2012)*, p. PD/P8-08. See http://www-naweb.iaea.org/napc/physics/FEC/FEC2012/papers/792_PDP808.pdf.

[24] D. K. Mansfield, A. L. Roquemore, T. Carroll, Z. Sun, J. S. Hu, L. Zhang, Y. F. Liang, X. Z. Gong, J. G. Li, H. Y. Guo, G. Z. Zuo, P. Parks, W. Wu, and R. Maingi, Nucl. Fusion **53**, 113023 (2013).

[25] Y. Liang, X. Z. Gong, K. F. Gan, E. Gauthier, L. Wang, M. Rack, Y. M. Wang, L. Zeng, P. Denner, A. Wingen, B. Lv, B. J. Ding, R. Chen, L. Q. Hu, J. S. Hu, F. K. Liu, Y. X. Jie, J. Pearson, J. P. Qian, J. F. Shan, B. Shen, T. H. Shi, Y. Sun, F. D. Wang, H. Q. Wang, M. Wang, Z. W. Wu, S. B. Zhang, T. Zhang, X. J. Zhang, N. Yan, G. S. Xu, H. Y. Guo, B. N. Wan, J. G. Li, and EAST Team, Phys. Rev. Lett. **110**, 235002 (2013).

[26] T. E. Evans, R. A. Moyer, K. H. Burrell, M. E. Fenstermacher, I. Joseph, A. W. Leonard, T. H. Osborne, G. D. Porter, M. J. Schaffer, P. B. Snyder, P. R. Thomas, J. G. Watkins, and W. P. West, Nat. Phys. **2**, 419 (2006).

[27] A. Loarte, Nat. Phys. **2**, 369 (2006).

[28] Y. Liang, H. R. Koslowski, P. R. Thomas, E. Nardon, B. Alper, P. Andrew, Y. Andrew, G. Arnoux, Y. Baranov, M. Bécoulet, M. Beurskens, T. Biewer, M. Bigi, K. Crombe, E. De La Luna, P. de Vries, W. Fundamenski, S. Gerasimov, C. Giroud, M. P. Gryaznevich, N. Hawkes, S. Hotchin, D. Howell, S. Jachmich, V. Kiptily, L. Moreira, V. Parail, S. D. Pinches, E. Rachlew, and O. Zimmermann, Phys. Rev. Lett. **98**, 265004 (2007).

[29] A. Kirk, E. Nardon, R. Akers, M. Bécoulet1, G. De Temmerman, B. Dudson, B. Hnat, Y. Q. Liu, R. Martin, P. Tamain, D. Taylor, and MAST Team, Nucl. Fusion **50**, 034008 (2010).

[30] W. Suttrop, T. Eich, J. C. Fuchs, S. Günter, A. Janzer, A. Herrmann, A. Kallenbach, P. T. Lang, T. Lunt, M. Maraschek, R. M. McDermott, A. Mlynek, T. Pütterich, M. Rott, T. Vierle, E. Wolfrum, Q. Yu, I. Zammuto, H. Zohm, and ASDEX Upgrade Team, Phys. Rev. Lett. **106**, 225004 (2011).

[31] P. T. Lang, A. Loarte, G. Saibene, L. R. Baylor, M. Becoulet, M. Cavinato, S. Clement-Lorenzo, E. Daly, T. E. Evans, M. E. Fenstermacher, Y. Gribov, L. D. Horton, C. Lowry, Y. Martin, O. Neubauer, N. Oyama, M. J. Schaffer, D. Stork, W. Suttrop, P. Thomas, M. Tran, H. R. Wilson, A. Kavin, and O. Schmitz, Nucl. Fusion **53**, 043004 (2013).

[32] M. Rack, "Modelling approach for helical current filaments induced by lower hybrid waves on EAST," Nucl. Fusion (submitted).

[33] A. Loarte, R. D. Monk, J. R. Martín-Solís, D. J. Campbell, A. V. Chankin, S. Clement, S. J. Davies, J. Ehrenberg, S. K. Erents, H. Y. Guo, P. J. Harbour, L. D. Horton, L. C. Ingesson, H. Jäckel, J. Lingertat, C. G. Lowry, C. F. Maggi, G. F. Matthews, K. McCormick, D. P. O'Brien, R. Reichle, G. Saibene, R. J. Smith, M. F. Stamp, D. Stork, and G. C. Vlases, Nucl. Fusion **38**, 331 (1998).

[34] A. Kallenbach, M. Balden, R. Dux, T. Eich, C. Giroud, A. Huber, G. P. Maddison, M. Mayer, K. McCormick, R. Neu, T. W. Petrie, T. Pütterich, J. Rapp, M. L. Reinke, K. Schmid, J. Schweinzer, S. Wolfe, ASDEX Upgrade Team, DIII-D Team, Alcator Team, and JET-EFDA Contributors, J. Nucl. Mater. **415**, S19 (2011).

[35] T. Eich, B. Sieglin, A. Scarabosio, W. Fundamenski, R. J. Goldston, A. Herrmann, and ASDEX Upgrade Team, Phys. Rev. Lett. **107**, 215001 (2011).

[36] R. J. Goldston, Nucl. Fusion **52**, 013009 (2012).

[37] B. LaBombard, Bull. Am. Phys. Soc. **58**, 367 (2013).

[38] S. C. Liu, L. M. Shao, S. J. Zweben, G. S. Xu, H. Y. Guo, B. Cao, H. Q. Wang, L. Wang, N. Yan, S. B. Xia, W. Zhang, R. Chen, L. Chen, S. Y. Ding, H. Xiong, Y. Zhao, B. N. Wan, X. Z. Gong, and X. Gao, Rev. Sci. Instrum. **83**, 123506 (2012).

[39] E. A. Belli and J. Candy, Phys. Plasmas **17**, 112314 (2010).

[40] L. L. Lao, H. E. St. John, Q. Peng, J. R. Ferron, E. J. Strait, T. S. Taylor, W. H. Meyer, C. Zhang, and K. I. You, Fusion Sci. Technol. **48**, 968 (2005).

[41] V. Rozhansky, P. Molchanov, I. Veselova, S. Voskoboynikov, A. Kirk, and D. Coster, Nucl. Fusion **52**, 103017 (2012).

[42] X. Q. Xu, B. Dudson, P. B. Snyder, M. V. Umansky, and H. Wilson, Phys. Rev. Lett. **105**, 175005 (2010).

[43] T. Y. Xia, X. Q. Xu, and P. W. Xi, Nucl. Fusion **53**, 073009 (2013).

[44] X. Q. Xu, P. W. Xi, A. Dimits, I. Joseph, M. V. Umansky, T. Y. Xia, B. Gui, S. S. Kim, G. Y. Park, T. Rhee, H. Jhang, P. H. Diamond, B. Dudson, and P. B. Snyder, Phys. Plasmas **20**, 056113 (2013).

[45] X. Q. Xu, B. D. Dudson, P. B. Snyder, M. V. Umansky, H. R. Wilson, and T. Casper, Nucl. Fusion **51**, 103040 (2011).

[46] P. A. Politzer, A. W. Hyatt, T. C. Luce, F. W. Perkins, R. Prater, A. D. Turnbull, D. P. Brennan, J. R. Ferron, C. M. Greenfield, J. Jayakumar, R. J. La Haye, C. C. Petty, and M. R. Wade, Nucl. Fusion **45**, 417 (2005).

[47] R. J. Hawryluk, "An empirical approach to Tokamak transport," in *Proceedings of the Course in Physics Close to Thermonuclear Conditions, Varenna, 1979* (Commission of the European Communities, Brussels, 1980), Vol. I, p. 19.

[48] R. V. Budny, R. Andre, G. Bateman, F. Halpern, C. E. Kessel, A. Kritz, and D. McCune, Nucl. Fusion **48**, 075005 (2008).

[49] S. C. Jardin, N. Pomphrey, and J. Delucia, J. Comput. Phys. **66**, 481 (1986).

[50] L. Degtyarev and V. Drozdov, Comput. Phys. Rep. **2**, 341 (1985).

[51] K. Itoh, M. Yagi, S.–I. Itoh, A. Fukuyama, and M. Azumi, Plasma Phys. Controlled Fusion **35**, 543 (1993).

[52] Y. Nakamura, K. Tobita, A. Fukuyama, N. Takei, Y. Takase, T. Ozeki, and S. C. Jardin, Nucl. Fusion **46**, S645 (2006).

[53] A. Pankin, D. McCune, R. Andre, G. Bateman, and A. Kritz, Comput. Phys. Commun. **159**, 157 (2004).

[54] D. W. Ignat, E. J. Valeo, and S. C. Jardin, Nucl. Fusion **34**, 837 (1994).

[55] M. Brambilla, Plasma Phys. Controlled Fusion **41**, 1 (1999).

[56] K. Matsuda, IEEE Trans. Plasma Sci. **17**, 6 (1989).